Gazing at crystal balls: Electron backscatter diffraction pattern analysis and cross correlation on the sphere

Ralf Hielscher[a,*], Felix Bartel[a], Thomas Benjamin Britton[b]

[a]*Fakultät für Mathematik, Technische Universität Chemnitz, 09107, Chemnitz, Germany*
[b]*Department of Materials, Imperial College London, London, SW7 2AZ, UK*

Abstract

We present spherical analysis of electron backscatter diffraction (EBSD) patterns with two new algorithms: (1) band localisation and band profile analysis using the spherical Radon transform; (2) orientation determination using spherical cross correlation. These new approaches are formally introduced and their accuracies are determined using dynamically simulated patterns. We demonstrate their utility with an experimental dataset obtained from ferritic iron. Our results indicate that the analysis of EBSD patterns on the surface of the sphere provides an elegant method of revealing information from these rich sources of crystallographic data.

Keywords: Electron diffraction; electron microscopy; geometrical projection; cross correlation; crystallography

Highlights

1. We present a method to approximate Kikuchi patterns by spherical functions.

2. We utilize the spherical Radon transformation to localise Kikuchi bands and to analyse their profile.

3. We develop a spherical cross correlation method for orientation determination from Kikuchi patterns.

4. All methods are speed optimised using fast Fourier algorithms on the sphere and the orientation space.

---

*Corresponding author
  Email addresses:* `ralf.hielscher@mathematik.tu-chemnitz.de` (Ralf Hielscher),
`b.britton@imperial.ac.uk` (Thomas Benjamin Britton)

1. Introduction

Electron backscatter diffraction (EBSD) is a popular microscopy technique used to reveal crystallographic information about materials. Automated, quantitative, robust, and precise interpretation of each electron backscatter pattern (EBSP) (aka Kikuchi pattern) has long been a major advantage of the technique [1], especially when compared to other methods, such as transmission electron microscopy (TEM) imaging and until recently [2] S(canning)TEM based mapping. To advance the EBSD technique further, it is advantageous to improve the quality of the information captured and simultaneously improve how we interpret each pattern. The latter motivates our present work, where we consider the patterns as images on the sphere and analyse them using the spherical Radon transform and spherical cross correlation. In particular, both algorithms may be utilized for automatic orientation determination and band shape analysis.

The majority of existing algorithms for the analysis of EBSP consider them in the gnomonic projection, i.e., as they are measured at a flat 2D capturing screen [3]. In this manuscript, we exploit the fact that the EBSP is generated from a point source and is, therefore, more properly rendered onto the surface of the sphere [4]. For band localisation this is advantageous as Kikuchi bands have parallel edges on the sphere, but hyperbolic edges when considered in the plane. For the cross correlation method, the advantage of the spherical representation originates from the fact that different orientations differ just by a rotation of the spherical Kikuchi pattern while their correspondence at a flat detector is more involved.

The EBSP is generated as electrons enter the sample, scatter, and dynamically diffract. For an introduction to conventional EBSD analysis, see the review article by Wilkinson and Britton [1]. In practice, diffracting electrons are captured using a flat screen inserted within the electron microscope chamber. The result of this dynamical diffraction process is the generation of an EBSP that contains bands of raised intensity which are called the "Kikuchi bands". The centre line of each band corresponds to a plane that contains the electron source point and is parallel to the diffracting crystal plane. The edges of the bands are two Kossel conic sections separated by 2θ. The dynamical diffraction process is explained in greater detail in the work of Winkelmann et al. [6]. The corresponding software provides us with high quality simulations that contain significant crystallographic information, such as the intensity profile near a zone axes. These simulated patterns more accurately reproduce the intensity

distributions found within experimentally captured patterns, as compared to simple kinematic models. This development has spurred an interest in using these patterns for direct orientation determination by pattern matching techniques [5].

The Hough transform has been used to render the bands within the EBSP as points within a transformed space for easy localisation using a computer [7]. In these conventional algorithms, it is assumed that the bands within the EBSP are near parallel. This renders localisation of the bands into the computationally simpler challenge of finding peaks of high intensity within a sparsely populated space. Unfortunately, within the gnomonic projection the edges of the bands are not parallel. Additionally, the Hough transform of the bands produces butterfly artefacts which makes precise and robust localisation of the bands challenging. However, if the bands are presented as rings on the surface of the sphere [4] there is potential to integrate intensity profiles more precisely. This is advantageous for geometries where there may be divergence of the bands (e.g. low voltage or where the pattern centre is less central).

To advance our analysis further, peak localisation and indexing may not be needed if we can efficiently directly compare and match the intensity distributions found within a high quality simulation against our experimental pattern. This can be performed with cross correlation (i.e. finding a peak in the associated cross correlation function), which underpins template matching based EBSD analysis, including the "dictionary indexing" method [5] and template matching approaches [8, 9].

Existing cross correlation methods [10, 5, 8, 9] are performed within the gnomonic projection of the detector. Hereby, each measured Kikuchi pattern $P = (P_{ij})$ is compared with a reference pattern $S(\boldsymbol{O}) = (S_{ij}(\boldsymbol{O}))$ according to a test orientation $\boldsymbol{O}$. The fit between both images is commonly measured by their correlation

$$C(P, S(\boldsymbol{O})) = \sum_{i,j} P_{ij} S_{ij}(\boldsymbol{O}) \tag{1.1}$$

where the sum is over all pixels in the pattern.

For template matching, reference patterns are tested according to multiple orientations. Sampling of the orientations is performed with a desired angular resolution (sufficient to find a peak and related to the ultimate angular sensitivity). This is computationally very expensive as the above sum has to be computed for a sufficiently large number of reference patterns $S(\boldsymbol{O}_m)$, $m = 1, \ldots, M$ to have a good estimate of the true orientation of the measured

Kikuchi pattern P. Recently, Foden et al. [8] have presented an alternative approach where a FFT-based cross correlation is combined with a subsequent orientation refinement step to interpolate between library patterns to provide a more computationally efficient method of template matching. However, that method still involves an expensive gnomonic based library search.

In this work we address this efficiency problem and perform the matching directly on the surface of the sphere. Therefore, we require only one spherical master pattern. In this paradigm different orientations results in different rotations of the spherical master pattern. The central idea of this paper is to represent the correlation function between the experimental Kikuchi pattern and all rotated versions of the spherical master pattern as a spherical convolution which can be computed using fast Fourier techniques.

In the case of plane images P and S it is well known [11] that the correlation image

$$C_{k,\ell} = \sum_{i,j} P_{ij} S_{i+k,j+\ell}$$

with respect to all shifts k, ℓ can be computed simultaneously using the fast Fourier transform $\mathcal{F}$. More precisely, we have

$$C = \mathcal{F}^{-1}(\mathcal{F}P \odot \mathcal{F}S)$$

where $\odot$ denotes the pointwise product. Such Fourier based algorithms have approximately square root the number of operations compared with direct algorithms.

The match between two spherical diffraction patterns can be measured through spherical cross correlation resulting in a function on orientation space. The position of the maximum peak of this function directly gives the desired misorientation of the experimental pattern with respect to the master pattern. In order to speed up the computation of the spherical cross correlation function we apply the same Fourier trick as explained above. In short, we compute spherical Fourier coefficients of the experimental and the master pattern, multiply them and obtain a series representation of the cross correlation function with respect to generalised spherical harmonics. Computation of the spherical Fourier coefficients and evaluation of the generalised spherical harmonics is done using the nonequispaced fast Fourier transform (NFFT) which is at the heart of the MTEX toolbox used for crystallographic texture analysis. The NFFT builds upon significant research generalising the FFT to non Euclidean domains, e.g. to the sphere, cf. [13, 14], or the orientation space cf. [15] and to apply them to problems

in quantitative texture analysis, cf. [16, 17, 18, 19]. Although our algorithms are theoretically fast the running times of our implementations are behind those of well established methods. The main reason for this is that our implementations are not yet optimised to take advantage of crystal symmetries, computing on the graphics card or any other kind of parallelisation. On the other hand, this keeps our proof of concept code very simple and allows for easy customisation.

2. Spherical diffraction patterns

The advantages of considering Kikuchi patterns as spherical functions have been explained very nicely by Day [4]. As an illustrative example of a Kikuchi pattern we consider a high quality dynamical simulation of α-Iron (BCC) generated within DynamicS (Bruker Nano GmbH) and project it onto the surface of the sphere (Figure 3.1a). The commercial program uses dynamical theory presented by Winkelmann et al. [6] to calculate the intensity of electrons in the resultant diffraction pattern.

In the case of experimental patterns, the diffraction sphere is not completely described as the detector does not subtend all diffraction angles (Figure 3.2). The amount of the sphere covered is described by the shape, size, and detector distance. For our algorithms the incomplete coverage causes two issues: (1) edge effects, which can be resolved by appropriate use of windowing functions; (2) incomplete Kikuchi bands which leads to different peak intensities in the spherical Radon transform. We will address these in more detail within Sec. 4.

3. Harmonic approximation on the sphere

Simulated as well as experimental Kikuchi patterns can be interpreted as diffraction intensities f_j with respect to discrete diffraction directions $\boldsymbol{\xi}_j$ that can be computed from the position within the pattern by the inverse gnomonic projection. For our algorithms, we are interested in approximating these intensities f_j by a smooth spherical function $f \colon \mathbb{S}^2 \to \mathbb{R}$, represented by a series expansion of the form

$$f(\boldsymbol{\xi}) = \sum_{n=0}^{N} \sum_{k=-n}^{n} \hat{f}(n,k) Y_n^k(\boldsymbol{\xi}), \tag{3.1}$$

such that $f(\boldsymbol{\xi}_j) \approx f_j$. Hereby, Y_n^k denotes the spherical harmonics which replace the exponential functions in the classical Fourier transform. Elegant introductions into harmonic analysis

|(a) simulated|(b) $N = 256$|(c) $N = 128$|(d) $N = 64$|
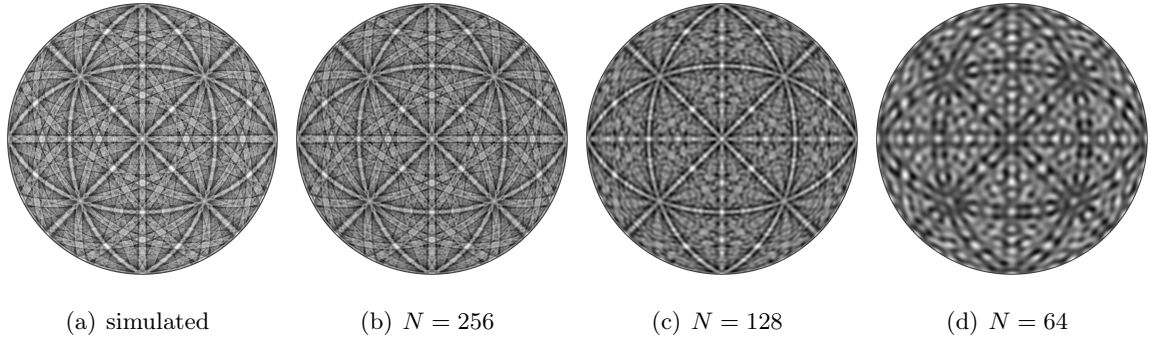
Figure 3.1 – Stereographic projection of the dynamically simulated Kikuchi pattern for iron (a) and its approximation by spherical harmonics with different harmonic degrees N.

on the sphere can be found in [? ?]. Similarly to the classical case many properties of the function f can be directly derived from its Fourier coefficients $\hat{f}(n,k)$. If we consider f as an image on the sphere (see Figure 3.1a), many image operations, like convolution, rotation, or differentiation, can be efficiently described in terms of the Fourier coefficients .

There exist several methods for determining the coefficients $\hat{f}(n,k)$ in (3.1) from discrete diffraction intensities $f(\boldsymbol{\xi}_j)$. Three of those will be introduced shortly: quadrature, interpolation, and approximation.

3.1. Quadrature

The quadrature based approach exploits the fact that the spherical harmonics Y_n^k form an orthonormal basis with respect to the inner product

$$\langle f_1, f_2 \rangle = \int_{\mathbb{S}^2} f_1(\boldsymbol{\xi}) \overline{f_2(\boldsymbol{\xi})} \, \mathrm{d}\boldsymbol{\xi}.$$

As a consequence, the expansion coefficients $\hat{f}(n,k)$ satisfy

$$\hat{f}(n,k) = \int_{\mathbb{S}^2} f(\boldsymbol{\xi}) \overline{Y_n^k(\boldsymbol{\xi})} \, \mathrm{d}\boldsymbol{\xi}.$$

Computing this integral numerically is called quadrature and leads to sums of the form

$$\hat{f}(n,k) \approx \sum_{j=1}^{J} \omega_j f(\boldsymbol{\xi}_j) \overline{Y_n^k(\boldsymbol{\xi}_j)}, \tag{3.2}$$

with the quadrature nodes $\boldsymbol{\xi}_j \in \mathbb{S}^2$ and quadrature weights $\omega_j \in \mathbb{R}$, $j = 1, \ldots, J$. The challenge is to find those nodes and weights such that the approximation is as good as possible. Good choices are discussed in [20, 21] and the references therein.

Evaluating the sum (3.2) for $n = 0, \ldots, N$ and $k = -n, \ldots, n$ directly would require $N^2 \cdot J$ numerical operations. Fortunately, this sum can be computed much faster using the nonequispaced fast Fourier transform [22] requiring only $N^2 \log N + J$ numerical operations.

The key parameter when approximating a spherical function by its harmonic series expansion is the cut-off frequency N. Figure 3.1 illustrates the effect of this cut-off frequency N when approximating a Kikuchi pattern. Our numerical experiments will show that a cut-off frequency of $N = 128$ provides enough detail to enable band detection and orientation determination by cross correlation with reasonable precision for a typical pattern.

The advantage of the quadrature based approach is its simplicity. This comes at the cost that the function values of f have to be known at the specific quadrature nodes $\boldsymbol{\xi}_j$, which can be true for simulated patterns but will not be true for experimental patterns.

3.2. Interpolation and approximation

If the function f to be approximated is given at discrete points $\boldsymbol{\xi}_j$, $j = 1, \ldots, J$, i.e., $f(\boldsymbol{\xi}_j) = f_j$, for which no quadrature rule is known we may compute the expansion coefficients $\hat{f}(n, k)$ by solving the system of linear equations

$$\sum_{n=0}^{N} \sum_{k=-n}^{n} \hat{f}(n,k) Y_n^k(\boldsymbol{\xi}_j) = f_j. \tag{3.3}$$

It should be noted that this system of linear equations may become ill conditioned, especially in the case that the number of interpolation nodes J equals the number $(N+1)^2$ of coefficients $\hat{f}(n, k)$. It is therefore recommended to consider the underdetermined or overdetermined problem and solve it using the normal equation of first or second kind, respectively.

Interpolation corresponds to the underdetermined case where the system of equations (3.3) has no unique solution. To restore uniqueness we search for coefficients solving (3.3) and simultaneously minimising some functional $\varphi(\hat{\boldsymbol{f}})$ which characterises the smoothness of f. Common choices are Sobolev norms of order $s > 0$,

$$\varphi(\hat{\boldsymbol{f}}) = \sum_{n=0}^{N} \sum_{k=-n}^{n} (n+1)^s \left| \hat{f}(n,k) \right|^2.$$

The solution of this constrained minimisation problem can be found by solving the corresponding normal equation of second kind. See also [23] for more details on the stability of spherical interpolation.

In the case of experimentally measured data it can be easier and more stable to solve an approximation problem instead of an interpolation problem, i.e. we are in the overdetermined case and the system of equations (3.3) must not have any solution. We therefore look for the coefficients $\hat{f}(n,k)$ which achieve the smallest error

$$F(\hat{f}) = \sum_{j=1}^{J} \left(\sum_{n=0}^{N} \sum_{k=-n}^{n} \hat{f}(n,k) Y_n^k(\boldsymbol{\xi}_j) - f_j \right)^2 + \lambda \sum_{n=0}^{N} \sum_{k=-n}^{n} (n+1) \left| \hat{f}(n,k) \right|^2$$

while decaying to zero quickly. Here the first summand measures the fitting of the approximation in the points $\boldsymbol{\xi}_j$ and the second summand is the regularisation term that measures the smoothness of the function and punishes noise. The weighting between these two terms is accomplished via the parameter λ which is often called regularisation parameter and has to be chosen such that there is balance between these two contradicting terms.

As an example, Figure 3.2 depicts an "experimental" Kikuchi pattern 3.2(a) together with a quadrature based 3.2(b) and approximation based 3.2(c) representation with respect to spherical harmonics. We observe that the approximation based approach leads to severe artefacts close to the detector boundaries. The reason is that harmonic functions are very bad in representing functions with hard jumps. This problem can be significantly relaxed by multiplying the data with a filter that generates a smooth decay from the values inside the detector to zero outside the detector. The resulting harmonic approximation is displayed in 3.2(d).

4. Spherical Radon transform based band detection

In conventional orientation determination from EBSD data the Kikuchi pattern is represented in the flat, gnomonic frame and summed up along all straight lines resulting in the Radon (or Hough) transform. Since in the Radon transform diffraction bands appear as local extrema they can be found by a peak detection algorithm. A severe problem of this approach is that due to the gnomonic projection bands, in the Kikuchi pattern, do not appear as straight features but have hyperbolic shape. As a consequence the local extrema are less sharp which negatively affects the accuracy and robustness of this approach. An alternative band analysis method which correctly uses the fact that the parallel bands on the surface of the sphere are well represented as hyperbolic sections in the gnomonic frame is incorporated in the 3D Hough transform [24].
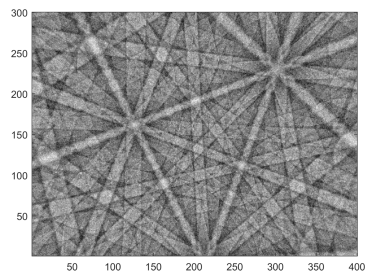
(a) Kikuchi pattern
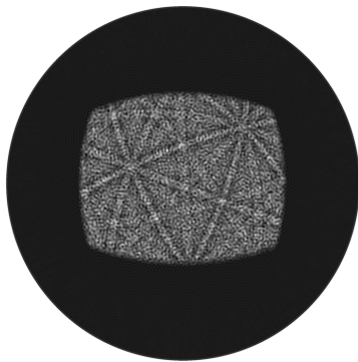
(b) quadrature
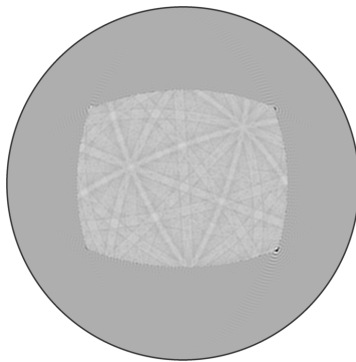
(c) approximation
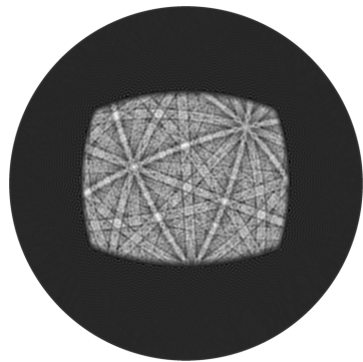

(d) with smooth cut-off function

Figure 3.2 – Spherical approximations of a simulated Kikuchi pattern at a detector corrupted by noise.

In this section we will make use of the fact that Kikuchi bands on the sphere are centered around great circles with edges formed by small circles that can be efficiently detected by a spherical Radon transform and its generalisations. Once sufficiently many bands are located the orientation can be determined by conventional indexing algorithms, e.g. with AstroEBSD [25].

4.1. The spherical Radon transform

The spherical Radon transform integrates a function on the sphere along all great circles, which is similar to how the ordinary Radon transform integrates an image along all lines. Such a great circle $\mathcal{C}$ on the sphere can be described as the set of all points $\boldsymbol{\xi} \in \mathbb{S}^2$ that are orthogonal to a given normal vector $\boldsymbol{\eta} \in \mathbb{S}^2$, i.e., $\mathcal{C}(\boldsymbol{\eta}) = \{\boldsymbol{\xi} \in \mathbb{S}^2 \mid \boldsymbol{\xi} \cdot \boldsymbol{\eta} = 0\}$. Accordingly the spherical Radon transform

$$g(\boldsymbol{\eta}) = \mathcal{R}f(\boldsymbol{\eta}) = \int_{\mathcal{C}(\boldsymbol{\eta})} f(\boldsymbol{\xi}) \, \mathrm{d}(\boldsymbol{\xi}) \tag{4.1}$$

of a spherical function $f \colon \mathbb{S}^2 \to \mathbb{R}$ is again a spherical function $g \colon \mathbb{S}^2 \to \mathbb{R}$.

The crucial point is now, that the Fourier representation of g can be computed straight forward from the Fourier coefficients $\hat{f}(n,k)$ of f, i.e., we have

$$g(\boldsymbol{\eta}) = \sum_{n=0}^{N} \sum_{k=-n}^{n} P_n(0) \hat{f}(n,k) Y_n^k(\boldsymbol{\eta}), \tag{4.2}$$

where $P_n(0)$ are the Legendre polynomials evaluated in the point 0. The practical use of this formula is that for computing the Radon transform of a spherical image, we do not need to average the pixel values along all great circles but, instead, compute the Fourier coefficients of the spherical image, multiply them with

$$P_n(0) = \begin{cases} (-1)^{n/2} \frac{(n-1)(n-3)\cdots 3 \cdot 1}{n(n-2)\cdots 4 \cdot 2}, & n \text{ is even} \\ 0, & n \text{ is odd} \end{cases}$$

and apply the spherical Fourier transform which gives us the spherical image of the Radon transform. For an image of $m \times m$ pixels the later algorithm using the nonequispaced fast spherical Fourier transform [14] is about m times faster.

Fig. 4.1a shows the spherical Radon transform of the dynamically simulated master pattern from Fig. 3.1. The circular features correspond to the bands in the Kikuchi pattern.

10

(a)

(b)
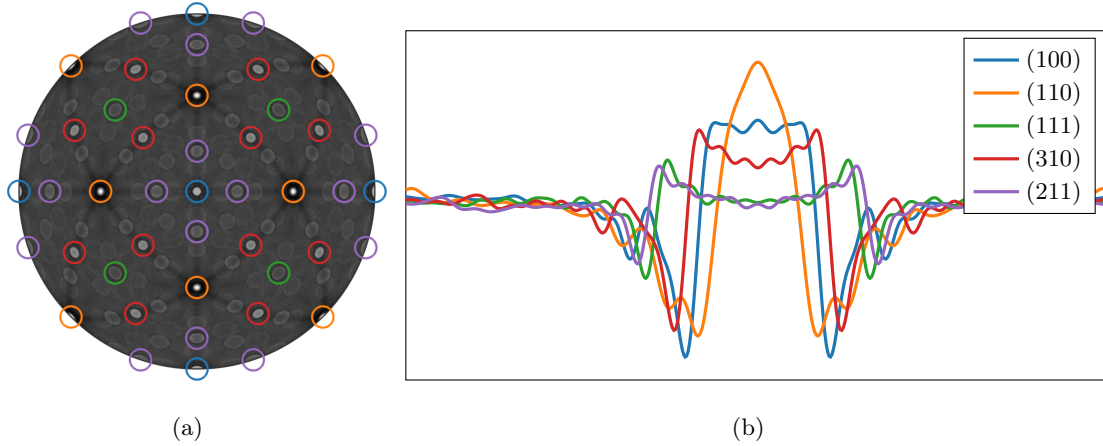
Figure 4.1 – (a) Spherical Radon transform of the master pattern (b) band profiles corresponding to different lattice planes.

4.2. Spherical convolution and band localisation

The brightness and sharpness of the Radon peaks is not uniform in Fig. 4.1a due to the different shape of the bands corresponding to the different lattice planes. To visualize and analyze the profile of the band, corresponding to a plane with normal vector $\boldsymbol{\eta} \in \mathbb{S}^2$, in more detail we integrate the spherical diffraction pattern f_{sim} in Fig. 3.1c with respect to all rotations $R_{\boldsymbol{\eta}}(\omega)$ about the plane normal $\boldsymbol{\eta}$, i.e.,

$$\Phi_{\boldsymbol{\eta}}(\boldsymbol{\xi}) = \int_0^{2\pi} f_{\text{sim}}(R_{\boldsymbol{\eta}}(\omega)\boldsymbol{\xi})\, \mathrm{d}\omega.$$

The resulting band profiles $\Phi_{\boldsymbol{\eta}}$ for the major bands are depicted in Fig. 4.1b.

Let us give a small site note on how those integrals can be computed efficiently from the Fourier coefficients $\hat{f}_{\text{sim}}(n, k)$ of the master pattern. In case the plane normal $\boldsymbol{\eta}$ coincides with the z-axis the profile $\Phi_{\boldsymbol{z}}$ is given by the Legendre series

$$\Phi_{\boldsymbol{z}}(\boldsymbol{\xi}) = \sum_{n=0}^N \hat{f}_{\text{sim}}(n, 0) P_n(\boldsymbol{\xi} \cdot \boldsymbol{z}). \tag{4.3}$$

In the general case of an arbitrary plane normal $\boldsymbol{\eta}$, it is sufficient to rotate f_{sim} such that the plane normal aligns with the z-axis and to proceed as above.

We may use our knowledge of these band profiles to identify specific bands within the experimental pattern using a spherical convolution

$$f \star \Phi(\boldsymbol{\eta}) = \int_{\mathbb{S}^2} f(\boldsymbol{\xi})\Phi(\boldsymbol{\xi} \cdot \boldsymbol{\eta})\, \mathrm{d}\boldsymbol{\xi}. \tag{4.4}$$

| (a) band (211) | (b) band (310) | (c) Gaussian | (d) modified Gaussian |
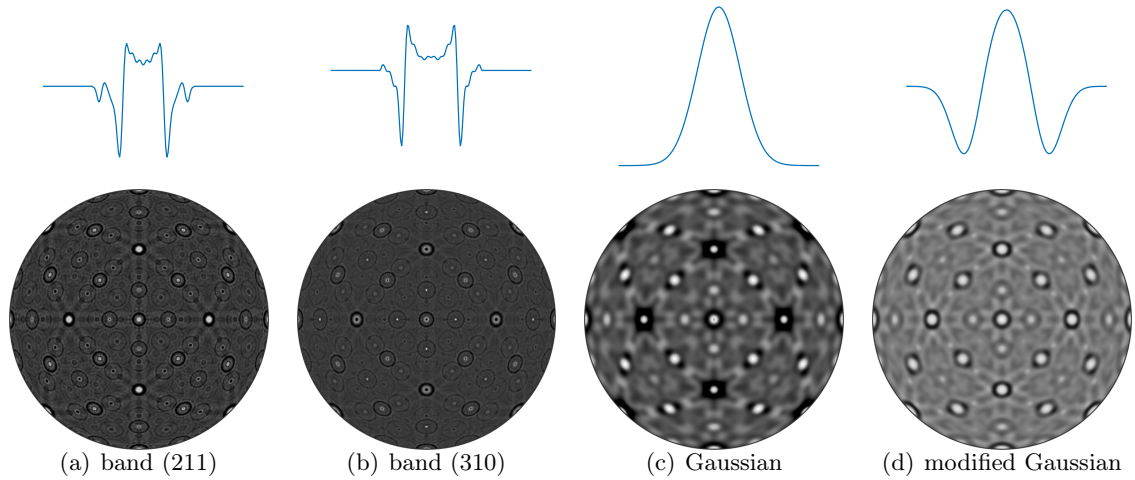
Figure 4.2 – Spherical convolution of the master pattern with different band profiles.

of the pattern f with a specific band profile Φ. The spherical convolution with a band profile can be seen as a generalisation of the spherical Radon transform. Indeed, choosing as the band profile $\Phi = \delta$ the delta distribution the spherical convolution $f \star \Phi = \mathcal{R}f$ coincides with the spherical Radon transform. On the other hand, it may also be interpreted as a generalisation of the butterfly mask [7] and the top hat filter [26] used in conventional Radon/Hough based EBSD.

In Fig. 4.2(a) and 4.2(b) the spherical convolutions of the master pattern with band profiles corresponding to planes (211) and (310) have been plotted. We observe extremely bright and sharp peaks at the corresponding band positions. The other bands are not as pronounced, as they match the convolution template less well.

In order find a template Ψ that reasonably fits all major bands we start with a Gaussian profile in Fig. 4.2(c) and modify it to

$$\Psi(\cos \omega) = \exp\Big(-\frac{(\omega - 90)^2}{9}\Big) - \exp\Big(-\frac{(\omega - 93)^2}{4}\Big) - \exp\Big(-\frac{(\omega - 87)^2}{4}\Big) \qquad (4.5)$$

in 4.2(d) which we will rely on in our subsequent analysis.

Lets close this section by the remark that the convolution $f \star \Phi$ can be computed as fast as the spherical Radon transform in Fourier space by the formula

$$f \star \Phi(\boldsymbol{\eta}) = \sum_{n=0}^{N} \sum_{k=-n}^{n} \hat{\Phi}(n) \hat{f}(n,k) Y_n^k(\boldsymbol{\eta}) \qquad (4.6)$$

where $\hat{\Phi}(n)$ denotes the Legendre coefficients of the band profile Ψ.

4.3. Peak detection

In the conventional Radon/Hough transform approach for band detection in Kikuchi patterns, the number of pixels in the Radon transform is approximately the same as in the input (resized) Kikuchi pattern. This limits the possible resolution of the orientations determined[1]. In contrast, when computing the spherical Radon transform according to (4.2) or the spherical convolution by (4.6) such a restriction to a grid of pixels does not exist. Instead, we can evaluate those sums for any normal vector $\boldsymbol{\eta}$. Since it would be way too time consuming to evaluate (4.2) or (4.6) at an arbitrarily fine grid, we propose a simultaneous steepest descent approach to find all local maxima.

The algorithm to find all peaks of a spherical function g is as follows: we start with a set of approximately equispaced points $\boldsymbol{\eta}_m$, $m = 1, \ldots, M$ on the sphere. Then we compute all the gradients $\nabla g(\boldsymbol{\eta}_m)$, $m = 1, \ldots, M$ of g according to the formulae

$$\partial_\rho g(\eta(\theta, \rho)) = \sum_{n=0}^{N} \sum_{k=-n}^{n} \mathrm{i} k \hat{g}(n, k) Y_n^k(\boldsymbol{\eta}),$$

$$\partial_\theta g(\eta(\theta, \rho)) = \sum_{n=0}^{N} \sum_{k=-n}^{n} k \hat{g}(n, k) Y_n^k(\boldsymbol{\eta}),$$

$$\nabla g(\eta) = \frac{1}{\sin \theta} \partial_\rho g(\boldsymbol{\eta}) \boldsymbol{e}_\rho(\boldsymbol{\eta}) + \frac{1}{\sin^2 \theta} \partial_\theta g(\boldsymbol{\eta}) \boldsymbol{e}_\theta(\boldsymbol{\eta})$$

(4.7)

using the fast spherical Fourier transform and maximize g locally along the lines

$$\boldsymbol{\eta}_m^1 = \boldsymbol{\eta}_m + \lambda_m^1 \nabla g(\boldsymbol{\eta}_m), \quad \lambda_m^1 \in [0, \pi).$$

This procedure is iterated and nodes $\boldsymbol{\eta}_m^\ell$ are found which converge for $k \to \infty$ to the local maxima of the function g. During the convergence, several of the nodes $\boldsymbol{\eta}_m^\ell$ will converge to the same maxima and, hence, can be merged into one node.

To illustrate this procedure we apply it to the simulated, noisy Kikuchi pattern in Fig. 4.3(a) from which we computed the convolution with the modified Gaussian profile (Fig. 4.2d) as depicted in Fig. 4.3(b). The diamond shaped artifact in the center corresponds no normal vectors of the bands that are completely outside the detector region. The four vertices of the diamond correspond the the edges of the detector region. Since, the detector region is known

---

[1]The resolution of Radon/Hough based approaches is a combination of the resolution of the Radon space, the quality of the diffraction patterns, and the number of bands successfully localised and indexed.
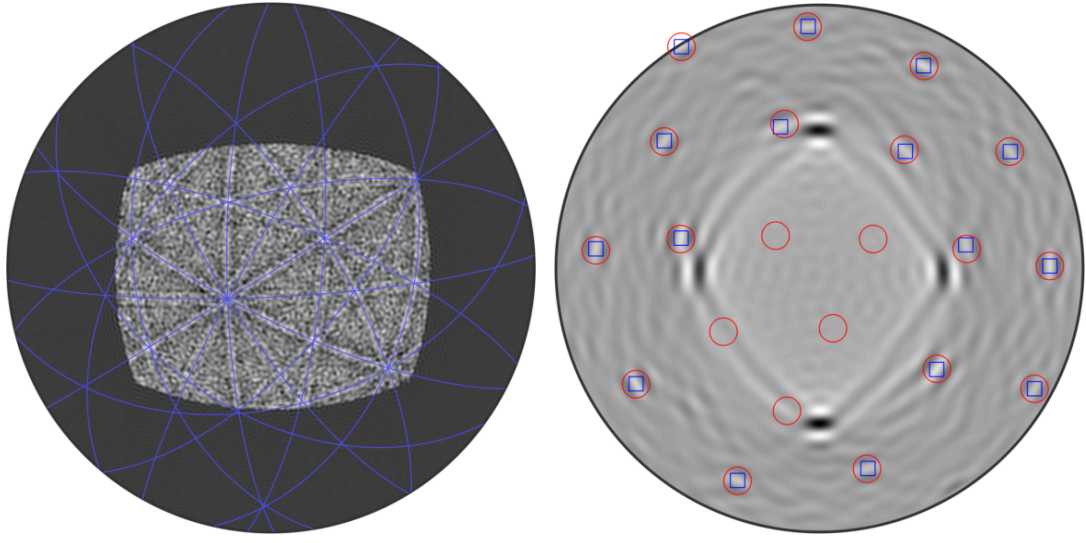
(a) spherical projection   (b) spherical convolution

Figure 4.3 – (a) Simulated, noisy Kikuchi pattern (b) spherical convolution with the band profile from Fig. 4.2(d). The red circles mark the theoretical normals of the major lattice bands and the blue square the detected peaks. The corresponding bands are marked by blue circles in left picture.

we could adapt our peak finding algorithm to ignore all peaks inside the diamond as well as its vertices. Due to the noise in the Kikuchi pattern the convolution with the modified Gaussian profile contains many minor peaks not associated to any lattice plane. Nevertheless, selecting simply the 16 brightest peaks (blue squares) found by our peak detection algorithm gave a very good coincidence with the theoretic positions of the major band normals (red circles). Obviously, the five red circles close to the diamond shaped artifact could not detected at all.

4.4. Orientation determination.

Once a certain number of bands has been detected in the Kikuchi pattern any of the well known indexing algorithms, e.g. [27, 25], can be used for determining the corresponding orientation. In this section we utilise AstroEBSD [25] and analyse the error distribution of the resulting orientation determination method.

To refresh, our spherical Radon transform based orientation determination method involves:

1. Project the experimental diffraction pattern onto the surface of the sphere

2. Approximate the discrete pattern by a spherical Fourier series as per equation (3.1).

3. Compute the spherical convolution (4.6) with a suitable band profile in Fourier space.

4. Detect the most pronounced peaks in the spherical convolution and search for their centres.

5. Use an indexing method (e.g. AstroEBSD) to index bands and ultimately determine the crystal orientation.

6. If needed, this crystal orientation can be transformed into another frame (e.g. from the detector frame to the sample frame).

This algorithms involves a couple of parameters which need to be adjusted carefully. In step 1, the pattern centre must be known. In step 2, we have to choose the harmonic cut-off frequency N, in step 3, a suitable band profile (which matches the bands expected in our lookup table), and in step 4, the number of iterations, the resolution of the initial search grid as well as the number bands which will passed in step 5 into the indexing algorithm.

For our BCC-iron patterns we select the modified Gaussian band profile (Fig. 4.2d), calibrated using our master pattern, and set the numbers of bands to 10.

Putting everything together we first verify our method with simulated noisy patterns. Therefore, we proceed as follows. First we select a random orientation $\boldsymbol{O}$. Then we dynamically simulate a corresponding Kikuchi pattern with 400×300 pixel and add noise as displayed in Fig. 4.3(a). We use this pattern to determine an orientation $\tilde{\boldsymbol{O}}$. Finally, we compute the misorientation between initial orientation $\boldsymbol{O}$ and the computed orientation $\tilde{\boldsymbol{O}}$. Histograms of these misorientation angles for different harmonic cut-off degrees N are depicted in Fig. 4.4. We determine that a mean accuracy of 0.1° can be obtained when the pattern centre is known exactly *a priori*.

In Sec. 6 we will demonstrate this orientation determination method with an experimental data set.

5. Spherical cross correlation based orientation determination

We have established that experimental and master pattern can be well represented by their harmonic expansion on the sphere and that this representation is useful for band detection. Now we present the use of this representation when computing the cross correlation between an experimental pattern with all possible rotations of a master pattern.
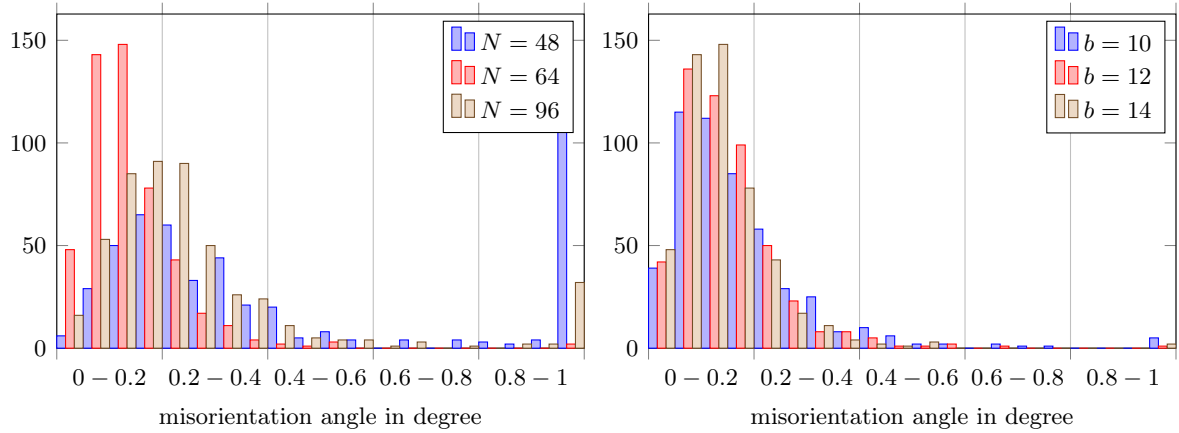
Figure 4.4 – Histograms of the misorientation between the original orientation and the orientation determined by spherical band detection. Left histogram fixes the number of bands $b = 14$ and varies the harmonic cut-off degrees N and right histogram fixes the harmonic cut-off degrees $N = 64$ and varies the number of bands b.

Template matching of EBSD patterns usually employs the following steps:

1. Simulate a dynamical master pattern of all orientation vectors.

2. Select a dense set of orientations $\boldsymbol{O}_m$, $m = 1, \ldots, M$.

3. Create a library of Kikuchi patterns S_{ij}^m with respect to all orientations $\boldsymbol{O}_m$, $m = 1, \ldots, M$ by rotating and projecting the master to the detector plane.

4. For a measured experimental pattern P_{ij} compute the cross correlations $C(m)$, $m = 1, \ldots, M$ with respect to all patterns S_{ij}^m within the library.

5. Select the orientation $\boldsymbol{O}_{\tilde{m}}$ with the largest cross correlation value $C(\tilde{m})$ as the indexed orientation.

The main advantage of this template matching based approach for orientation determination is that it takes into account all diffraction pattern features and does not reduce the analysis to a simple "geometry" based problem of localising and indexing the bands. This provides the potential that this method is more robust to noise.

The main disadvantage of the template matching approach is that reprojection of the master pattern for a dense population of orientation space is memory intensive and that the repeated computation of the cross correlation of each experimental pattern with all patterns of the library is computationally expensive.

To overcome this shortcoming, we transfer the template matching based approach to our spherical setting and make use of the fast Fourier transform on the rotation group. This allows us to compute the spherical cross correlations simultaneously for all orientations $\boldsymbol{O}_m$, $m = 1, \ldots, M$ which is much faster than by a pixel by pixel based formula.

5.1. Spherical cross correlation

We start by representing both the simulated pattern as well as the experimental pattern by expansions in spherical harmonics

$$f_{\text{sim}}(\boldsymbol{h}) = \sum_{n=0}^{N} \sum_{k=-n}^{n} \hat{f}_{\text{sim}}(n, k) Y_n^k(\boldsymbol{h}) \tag{5.1}$$

$$f_{\text{exp}}(\boldsymbol{r}) = \sum_{n=0}^{N} \sum_{k'=-n}^{n} \hat{f}_{\text{exp}}(n, k') Y_n^{k'}(\boldsymbol{r}) \tag{5.2}$$

as discussed in Sec. 3. Note, that the simulated pattern f_{sim} is usually represented with respect to crystal coordinates, while the experimental pattern f_{exp} is represented with respect to detector coordinates. Let $\boldsymbol{O}$ be the exact crystal orientation of the experimental pattern, i.e., $\boldsymbol{r} = \boldsymbol{O}\boldsymbol{h}$. Then the basic assumption of the pattern matching approach is that the simulated pattern transformed into the specimen reference frame gives a good approximation of the experimental pattern modulo a scaling factor $\alpha \in \mathbb{R}$, i.e.

$$f_{\text{exp}}(\boldsymbol{r}) \approx \alpha f_{\text{sim}}(\boldsymbol{O}^{-1}\boldsymbol{r}).$$

The similarity of two spherical functions modulo a rotation $\boldsymbol{O}$ can be measured by the spherical cross correlation, which is defined as the integral of the product of both functions over the entire sphere

$$C(f_{\text{sim}}, f_{\text{exp}})(\boldsymbol{O}) = \int_{\mathbb{S}^2} f_{\text{sim}}(\boldsymbol{O}^{-1}\boldsymbol{r}) f_{\text{exp}}(\boldsymbol{r}) \, \mathrm{d}\boldsymbol{r} = \int_{\mathbb{S}^2} f_{\text{sim}}(\boldsymbol{h}) f_{\text{exp}}(\boldsymbol{O}\boldsymbol{h}) \, \mathrm{d}\boldsymbol{h}. \tag{5.3}$$

In order to evaluate these integrals numerically one could make use of a spherical quadrature rule with nodes $\boldsymbol{h}_n \in \mathbb{S}^2$ and weights $\omega_n > 0$, $n = 1, \ldots, N$, cf. Sec. 3.1, which leads to the sum

$$C(f_{\text{sim}}, f_{\text{exp}})(\boldsymbol{O}) \approx \sum_{n=1}^{N} \omega_n f_{\text{sim}}(\boldsymbol{h}_n) f_{\text{exp}}(\boldsymbol{O}\boldsymbol{h}_n). \tag{5.4}$$

This sum does not require to pre-compute and store a dictionary of simulated patterns. Instead it is sufficient to store the simulated master pattern f_{sim} at the quadrature nodes $\boldsymbol{h}_n$ and transform each experimental pattern to the sphere. Furthermore, it can be evaluated at arbitrary orientations $\boldsymbol{O}$, i.e, we are not restricted to any grid in the orientation space.

17

5.2. Fast evaluation of the spherical cross correlation

A critical disadvantage of the template matching approach are its high computational costs. Indeed, evaluating the cross correlation function (1.1) at a dense set of M orientations for patterns with N^2 points requires $M \cdot N^2$ numerical operations. Evaluating the spherical cross correlation function (5.4) directly would lead to the same amount of numerical operations. In this section we show how fast Fourier techniques on the orientation space can be exploited to speed up this computation to only $N^3 \log N + M$ numerical operations.

The idea is to use the following important relationship between spherical harmonics Y_n^k and Wigner-D functions $D_n^{k,k'}$, cf. [16],

$$D_n^{k,k'}(\boldsymbol{O}) = \int_{\mathbb{S}^2} Y_n^k(\boldsymbol{O}\boldsymbol{r})\overline{Y_n^{k'}(\boldsymbol{r})} \, \mathrm{d}\boldsymbol{r}$$

which allows us to rewrite the series expansion of the rotated simulated pattern as

$$f_{\mathrm{sim}}(\boldsymbol{O}^{-1}\boldsymbol{r}) = \sum_{n=0}^{N} \sum_{k=-n}^{n} \sum_{k'=-n}^{n} D_n^{k,k'}(\boldsymbol{O})\hat{f}_{\mathrm{sim}}(n,k')Y_n^{k'}(\boldsymbol{r}). \tag{5.5}$$

Inserting the series expansions (5.2) and (5.5) into the correlation integral (5.3) and making use of the orthogonality of the spherical harmonic Y_n^k we end up with

$$C(f_{\mathrm{sim}}, f_{\mathrm{exp}})(\boldsymbol{O}) = \sum_{n=0}^{N} \sum_{k,k'=-n}^{n} \hat{f}_{\mathrm{sim}}(n,k)\hat{f}_{\mathrm{exp}}(n,k')D_n^{k,k'}(\boldsymbol{O}) \tag{5.6}$$

$$= \sum_{n=0}^{N} \sum_{k,k'=-n}^{n} \hat{C}(n,k,k')D_n^{k,k'}(\boldsymbol{O}), \tag{5.7}$$

where we have set $\hat{C}(n,k,k') = \hat{f}_{\mathrm{sim}}(n,k)\hat{f}_{\mathrm{exp}}(n,k')$. The latter sum (5.7) is known as the Fourier transform on the rotation group and can be evaluated at M arbitrary orientations $\boldsymbol{O}_m$ using only $N^3 \log N + M$ numerical operations by the algorithm described in [15].

In order to illustrate our approach we have chosen a random orientation $\boldsymbol{O}$ and defined the function $f_{\mathrm{exp}}(\boldsymbol{r}) = f_{\mathrm{sim}}(\boldsymbol{O}^{-1}\boldsymbol{r})$ as a rotated version of our master pattern. In a second step we approximated both patterns by expansions into spherical harmonics up to cut-off degree $N = 512$. Finally, we calculated the spherical cross correlation function $C(f_{\mathrm{sim}}, f_{\mathrm{exp}})$ as a function of the misorientation from the initial orientation $\boldsymbol{O}$ for different, smaller, cut-off degrees N. The results are depicted in Fig. 5.1a. We observe that a cut off degree $N = 64$ gives a good localisation of the peak position close to the true orientation.
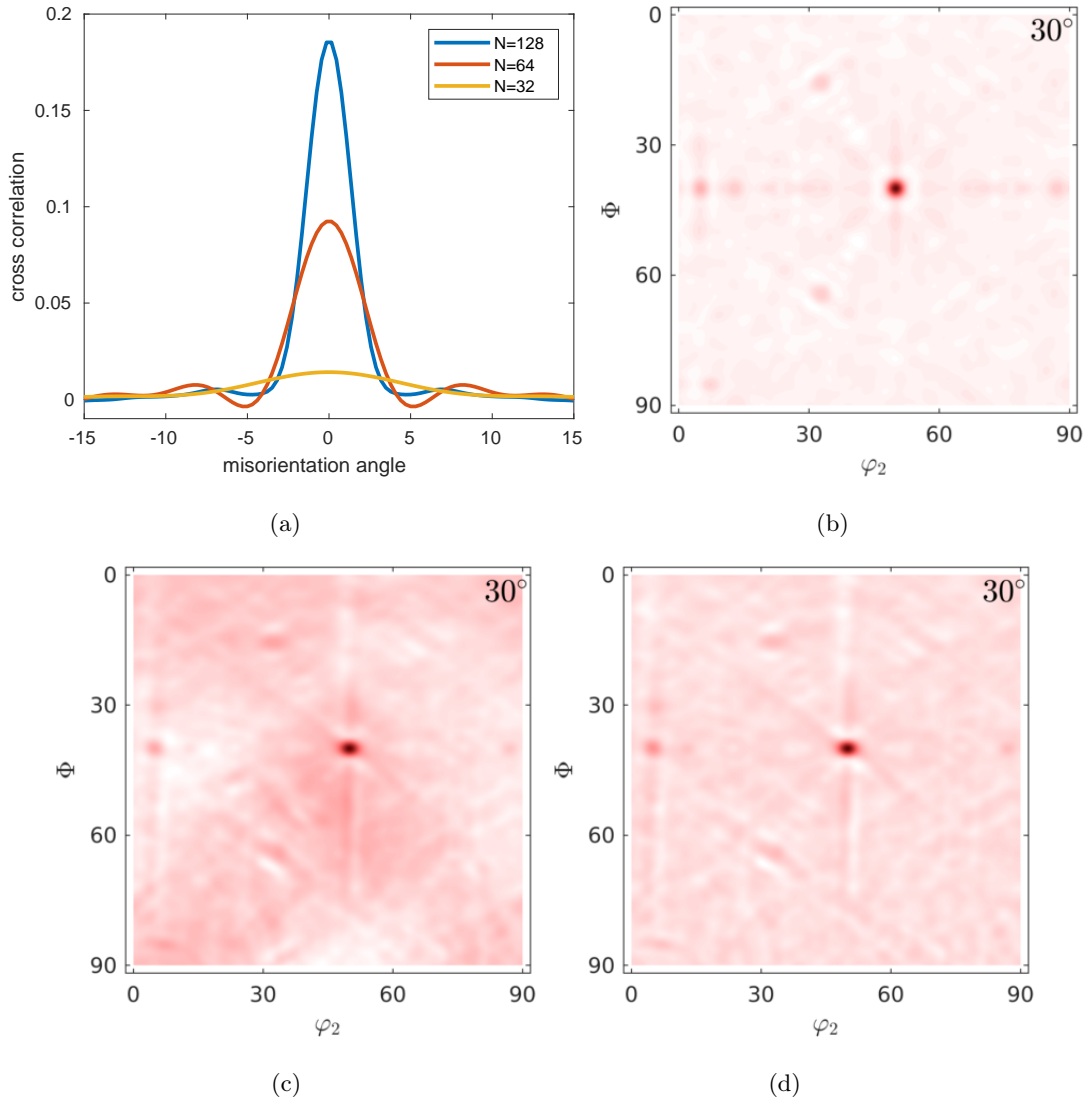
Figure 5.1 – Spherical cross correlation: (a) as a function of the misorientation angle from the exact orientation with respect to different harmonic cut-off parameters N; (b) as a section through the Euler space showing the dominant peak (dark red) at the position of the exact match; (c) the same section but with an "experimental" pattern, showing the artifacts due to the incomplete coverage of the sphere by the detector window; (d) the corrected cross correlation function $C(\boldsymbol{O})$ according to (5.8).

5.3. Correction

In the previous section we have assumed that the test pattern f_{exp} is known at the entire sphere. In practice, however, only the projection of the detector back to the sphere is known. This causes low frequency artifacts in the cross correlation function as depicted in Fig. 5.1c.

Luckily, these artefacts can be computed explicitly as the spherical cross correlation $C(f_{\text{sim}}, \chi)$ between the simulated Kikuchi pattern f_{sim} on the sphere and the cut-off function χ of the detector region projected to the sphere. The final difference

$$C(\boldsymbol{O}) = C(f_{\text{sim}}, f_{\text{exp}})(\boldsymbol{O}) - \frac{\int_{\mathbb{S}^2} f_{\text{exp}}}{\int_{\mathbb{S}^2} \chi} C(f_{\text{sim}}, \chi)(\boldsymbol{O}) \tag{5.8}$$

is depicted in 5.1(d).

5.4. Peak detection

Peak detection for functions of the form (5.7) can be implemented in a similar manner as explained in Sec. 4.3 for spherical functions since the gradient can again be written as a sum with respect to Wigner-D functions. However, in the present case we are only interested in finding the global maximum (and not many local maxima). This makes it efficient to evaluate the corrected cross correlation function (5.8) on a fixed and uniformly spaced grid of orientations $\boldsymbol{O}_m$, $m = 1, \ldots, M$ with resolution $\delta^{(1)} \approx 2°$ and choose the orientation $\boldsymbol{O}_{\tilde{m}}$ with maximum function value $C(\boldsymbol{O}_{\tilde{m}})$. In a second step we choose a local grid around the orientation $\boldsymbol{O}_{\tilde{m}}$ with radius $\delta^{(1)}$ and resolution $\delta^{(2)} \approx 0.1°$ and repeat the calculation. The global resolution needs to be chosen such that no peak falls between the grid points.

5.5. Accuracy determination for spherical cross correlation

We perform a numerical experiment to test the accuracy of our spherical cross correlation algorithm and optimise crucial parameters such as the harmonic cut-off degree N as well as the resolutions $\delta^{(1)}$ and $\delta^{(2)}$ of the global and local search grids:

1. Compute a spherical Fourier series approximation f_{sim} of a dynamically simulated master pattern as described in Sec. 3.2.

2. Generate random crystal orientation $\boldsymbol{O}$ and simulate a corresponding "experimental Kikuchi pattern" by projecting the master pattern to a virtual detector and adding Poisson distributed noise.
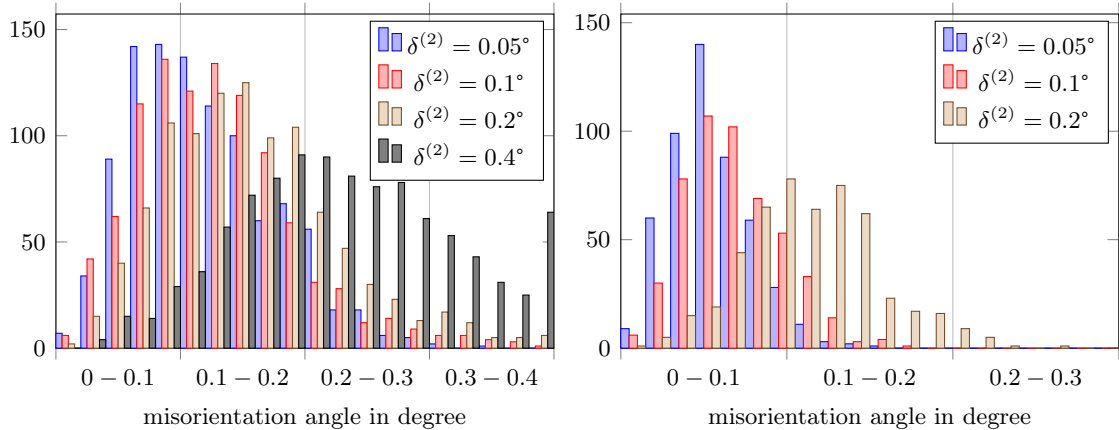
Figure 5.2 – Misorientation angle histograms between the "true" random orientation used for simulating the diffraction pattern and the orientation determined by spherical cross correlation. Left histogram fixes harmonic cut-off bandwidth $N = 48$ and right histogram $N = 64$. Only the resolution $\delta^{(2)}$ of the refined grid is given. The corresponding resolution of the global grid can be found in Table 5.1.

3. Project the noisy "experimental pattern" back to the sphere, multiply it by the mask φ and approximate the product by a spherical Fourier series f_{exp}.

4. Evaluate the corrected spherical cross correlation function $C(\boldsymbol{O}_m)$ between f_{sim} and f_{exp} at the grid orientations $\boldsymbol{O}_m$.

5. Determine the grid orientation $\boldsymbol{O}_{\tilde{m}}$ with the largest cross correlation value.

6. Compute the misorientation angle between the initial random orientation $\boldsymbol{O}$ and the computed orientation $\boldsymbol{O}_{\tilde{m}}$.

This numerical experiment has been run 500 times for different choices of the harmonic cut-off bandwidths N and the different resolutions of the search grid $\boldsymbol{O}_m$. Table 5.1 summarises the parameters, the run times and the achieved precision. Full histograms of the misorientation angles are depicted in Figure 5.2.

We observe that a global resolution $\delta^{(1)} = 5°$ is too coarse as it leads to about 5 percent completely mis-indexed patterns. For all other parameter choices we obtain reasonable angular precision up to 0.05° with a speed of one pattern per second on an ordinary laptop without any graphic card support.

21

cut-off	global search grid		local search grid			speed	precision	
N	res. $\delta^{(1)}$	points M_1	radius	res. $\delta^{(2)}$	points M_2	pattern/s	median	std
48	5°	4 958	5°	0.4°	9 106	1.8	0.22	4.56
48	2.5°	39 565	2.5°	0.2°	9 128	1.5	0.15	0.07
48	1.5°	183 035	1.5°	0.1°	14 005	1.3	0.12	0.06
48	1.5°	183 035	1.5°	0.05°	112 514	1.1	0.11	0.06
64	2.5°	39 565	2.5°	0.2°	9 128	1.4	0.11	0.04
64	1.5°	183 035	1.5°	0.1°	14 005	1.2	0.06	0.03
64	1.5°	183 035	1.5°	0.05°	112 514	1.0	0.05	0.02

Table 5.1 – Indication of computational costs and associated precision for spherical cross correlation. Times are measured on an ordinary laptop.

6. Experimental demonstration

We test our two spherical algorithms using the demonstration α-Iron data set as used in Britton et al. [25] for conventional indexing using a planar Radon transform and the AstroEBSD indexing algorithm. This data can be found on Zenodo `https://zenodo.org/record/1214829` and consists of a 9 130 point EBSD pattern map. The AstroEBSD background correction was used with operations: hot pixel correction; resize to 300 pixels wide; low frequency Gaussian background division (sigma = 4), performed independently on each detector half, circular radius cropping to 0.95 of the pattern width. All peak ID based indexing was performed using the iron phase file, with the top 10 bands used in the analysis. The flat Radon transform based analysis was performed with 1 degree theta resolution and up to 13 peaks were sought. The pattern centre was optimised by searching for the minimum weighted mean angular error using a 10×10 grid array. The spherical Radon transform based orientation determination was performed using the idealised profile given in (4.5) and the spherical cross correlation based orientation determination was performed using the harmonic cut-off frequency $N = 64$ and resolutions $\delta^{(1)} = 1.5°$, $\delta^{(2)} = 0.1°$ for the global, respective, local search grid. Results are presented in Fig. 6.1. The orientations are by all three method reasonably recovered. The smoothness in the axis-angle plots are similar, where the spherical method performs slightly better near grain boundaries and the spherical cross correlation method is

significantly more robust near grain boundaries.

7. Discussion

In this manuscript, we demonstrated that considering EBSD patterns as spherical images allows for elegant algorithms for band detection, band analysis and cross correlation. The reason behind this elegance is the fact that in its spherical representation symmetry operations and misorientations are simple rotations of the Kikuchi pattern.

Beside being elegant these algorithms can be implemented using fast Fourier techniques which makes them at least theoretically fast. In practice, our algorithms do not yet meet the speed of highly optimized implementations of standard Hough transform based indexing algorithms. The reason for this is that our algorithms are not yet parallelized, do not take advantage of symmetries and are mainly implemented with readability in mind.

Based on spherical band detection and spherical cross correlation we presented two new methods for orientation determination from Kikuchi pattern. In numerical experiments with noisy, simulated as well as experimental patterns we achieved an accuracy of up to 0.1 degree. Clearly, this accuracy depends on the noise level and the resolution of the provided EBSD pattern. A more precise relationship between noise level and resolution on the one side and achievable accuracy on the other side is subject of further research. Our examples on the iron data set demonstrated that our algorithm is more robust then conventional flat Radon transform based approaches.

Another advantage of the spherical analysis is that spherical convolution can used to extract specific bands according to their profile. Furthermore, those profiles can be efficiently computed from experimental patterns using formula (4.3) and then be explored with respect to shape and symmetry. This has the potential to better understand the asymmetry created either by an improper pattern centre [28], a subtle changes in the lattice [24], and band asymmetry [29, 30].

An important assumption of the spherical method is that we know the pattern centre *a priori*. The pattern centre is important for our analysis, as an incorrect pattern centre will introduce a distortion on the rendering of patterns on the sphere and the band edges would no longer be parallel. Computationally it can be expensive to optimise the pattern centre based upon this constraint, but there have been suggestions in the literature that centre on

inverse pole figure (IPF) colouring   axis angle colouring

2D Radon

spherical Radon

spherical cross correlation

color keys

$[\bar{1}11]$

$[001]$ $[011]$

upper   lower
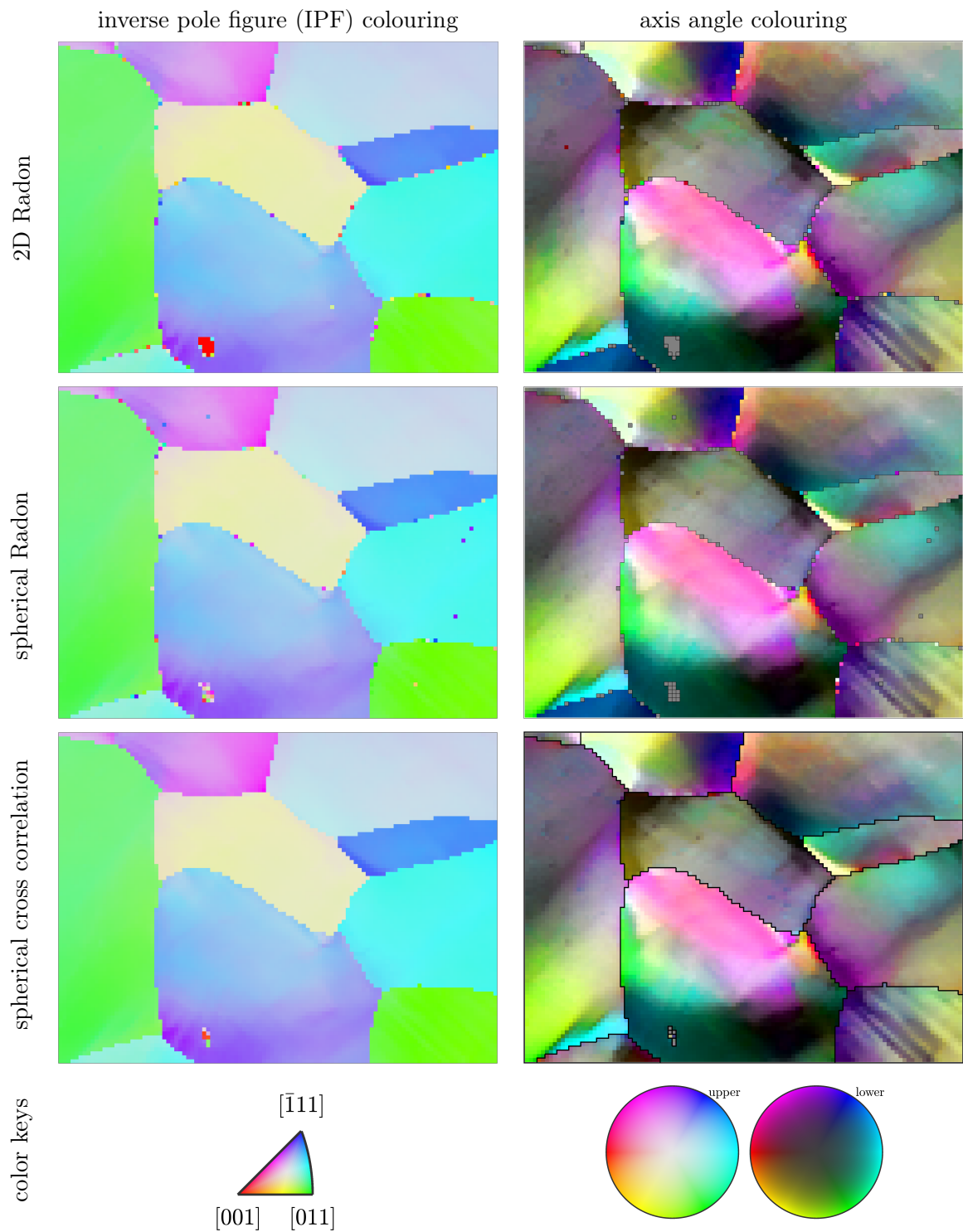
Figure 6.1 – Demonstration α-iron data indexed using 2D based Radon transform band localisation and AstroEBSD indexing, spherical Radon transform band localisation and AstroEBSD indexing, and spherical cross correlation. The IPF colour key is with respect to the horizontal axis. The axis-angle colour key is taken with respect to the mean grain orientation and each key has a radius of 5°.

24

this idea (e.g. the 3D Hough [24] and one of the methods of the BYU group [28] in attempting absolute strain measurement with high resolution EBSD). If we assume that we know, or can measure, the pattern centre with reasonable precision with standard methods (e.g. just using the 2D Radon based pattern centre measurements available within commercial or open-source software such as AstroEBSD [25]), then we can perform re-projection and gain reasonable indexing success which is demonstrated with the example iron data set shown with this work. Perhaps more excitingly, it is likely that the spherical approach will prove useful when less conventional capture geometries are used, as the divergence of the Kossel cones is naturally encoded when the pattern is projected onto the sphere. For instance, it is well known that this divergence has caused significant problems when analysing transmission Kikuchi patterns when the pattern centre no longer located within the detector screen.

8. Conclusion

We have outlined and demonstrated methods to perform analysis of EBSD patterns in a spherical frame. We can summarise our conclusions as:

- Simulated as well as experimental Kikuchi patterns can be well approximated by spherical functions. These approximations can be computed efficiently using the fast spherical Fourier transform.

- The choice of a suitable harmonic cut-off frequency is crucial for the approximation process.

- The spherical Radon transform and spherical convolution are efficient methods for band detection in Kikuchi pattern.

- The spherical approximation allows for an efficient method for extracting band profiles.

- The spherical cross correlation is an efficient method for determining the orientation of a Kikuchi pattern by comparing it with a rotated versions of a master pattern.

- The spherical Radon transform, spherical convolutions, as well as spherical cross correlation can be efficiently computed using fast Fourier transforms on the sphere and the rotation group.

- Spherical approximation, the spherical Radon transform, spherical convolution and spherical cross correlation can be adapted to work well with patterns that do not cover the entire sphere as it is typical for experimental pattern measured at a flat detector.

- In our numerical experiments with simulated, noisy Kikuchi patterns the spherical Radon transform based methods as well as the spherical cross correlation based methods for orientation determination achieved a precision of $< 0.1°$.

9. Data statement

The example iron data set can be found on Zenodo (https://doi.org/10.5281/zenodo.1214828). Upon article acceptance the full code for this manuscript will be released to Zenodo.

Acknowledgements

References

[1] A. J. Wilkinson, T. B. Britton, Strains, planes, and ebsd in materials science, Materials Today 15 (9) (2012) 366–376. `doi:Doi10.1016/S1369-7021(12)70163-3`.
URL `<GotoISI>://WOS:000310422900015`

[2] E. Rauch, J. Portillo, S. Nicolopoulos, D. Bultreys, S. Rouvimov, P. Moeck, Automated nanocrystal orientation and phase mapping in the transmission electron microscope on the basis of precession electron diffraction, Zeitschrift für Kristallographie - Crystalline Materials 225. `doi:10.1524/zkri.2010.1205`.
URL `https://doi.org/10.1524/zkri.2010.1205`

[3] B. Adams, S. Wright, K. Kunze, Orientation imaging: The emergence of a new microscopy, Metallurgical Transactions A 24 (4) (1993) 819–831. `doi:DOI10.1007/BF02656503`.
URL `https://link.springer.com/article/10.1007/BF02656503`

[4] A. Day, Spherical ebsd, Journal of Microscopy 409. `doi:10.1111/j.1365-2818.2008.02011.x`.

[5] Y. H. Chen, S. U. Park, D. Wei, G. Newstadt, M. A. Jackson, J. P. Simmons, M. De Graef, A. O. Hero, A dictionary approach to electron backscatter diffraction indexing, Microsc Microanal 21 (3) (2015) 739–52. `doi:10.1017/S1431927615000756`.
URL `https://www.ncbi.nlm.nih.gov/pubmed/26055190`

[6] A. Winkelmann, C. Trager-Cowan, F. Sweeney, A. P. Day, P. Parbrook, Many-beam dynamical simulation of electron backscatter diffraction patterns, Ultramicroscopy 107 (4-5) (2007) 414–421. `doi:10.1016/j.ultramic.2006.10.006`.
URL `<GotoISI>://WOS:000244373700018`

[7] N. Krieger Lassen, Automatic localisation of electron backscattering pattern bands from hough transform, Materials Science and Technology 12 (10) (1996) 837–843. `doi:DOI10.1179/mst.1996.12.10.837`.
URL `https://doi.org/10.1179/mst.1996.12.10.837`

[8] A. Foden, D. Collins, A. Wilkinson, T. Britton, Indexing electron backscatter diffraction patterns with a refined template matching approach, ArXiv Preprint.
URL `https://arxiv.org/abs/1807.11313`

[9] A. J. Wilkinson, D. M. Collins, Y. Zayachuk, R. Korla, A. Vilalta-Clemente, Applications of multivariate statistical methods and simulation libraries to analysis of electron backscatter diffraction and transmission kikuchi diffraction datasets, ArXiv Preprint.
URL `https://arxiv.org/abs/1806.02087`

[10] A. J. Wilkinson, G. Meaden, D. J. Dingley, High-resolution elastic strain measurement from electron backscatter diffraction patterns: New levels of sensitivity, Ultramicroscopy 106 (4-5) (2006) 307–313. `doi:10.1016/j.ultramic.2005.10.001`.
URL `<GotoISI>://WOS:000236042300008`

[11] P. Anuta, Spatial registration of multispectral and multitemporal digital imagery using fast fourier transform techniques, IEEE Transactions on Geoscience Electronics 8 (4) (1970) 353–368. `doi:10.1109/TGE.1970.271435`.

[12] E. W. Weisstein, Cross-correlation theorem, http://mathworld.wolfram.com/Cross-CorrelationTheorem.html, accessed: 2018-05-28.

[13] S. Kunis, A note on stability results for scattered data interpolation on euclidean spheres, Advances in Computational Mathematics 30 (4) (2009) 303–314. `doi:10.1007/s10444-008-9069-4`.
URL `<GotoISI>://WOS:000264513100001`

[14] S. Kunis, D. Potts, Fast spherical fourier algorithms, Journal of Computational and Applied Mathematics 161 (1) (2003) 75–98. `doi:10.1016/S0377-0427(03)00546-6`.
URL `<GotoISI>://WOS:000186545000005`

[15] D. Potts, J. Pestin, A. Vollrath, A fast algorithm for non equispaced fourier transforms on the rotation group, Numer. Algorithms 52 (2009) 355–384.

[16] R. Hielscher, D. Potts, J. Prestin, H. Schaeben, M. Schmalz, The radon transform on so(3): a fourier slice theorem and numerical inversion, Inverse Problems 24 (2). `doi:Artn02501110.1088/0266-5611/24/2/025011`.
URL `<GotoISI>://WOS:000254375500012`

[17] R. Hielscher, J. Prestin, A. Vollrath, Fast summation of functions on the rotation group, Mathematical Geosciences 42 (7) (2010) 773–794. `doi:10.1007/s11004-010-9281-x`.
URL `<GotoISI>://WOS:000281859900004`

[18] D. Mainprice, F. Bachmann, R. Hielscher, H. Schaeben, Descriptive tools for the analysis of texture projects with large datasets using mtex: strength, symmetry and components, Rock Deformation from Field, Experiments and Theory: A Volume in Honour of Ernie Rutter 409 (2015) 251–271. `doi:10.1144/Sp409.8`.
URL `<GotoISI>://WOS:000367998600014`

[19] D. Mainprice, F. Bachmann, R. Hielscher, H. Schaeben, G. E. Lloyd, Calculating anisotropic piezoelectric properties from texture data using the mtex open source pack-

age, Rock Deformation from Field, Experiments and Theory: A Volume in Honour of Ernie Rutter 409 (2015) 223–249. `doi:10.1144/Sp409.2`.
URL `<GotoISI>://WOS:000367998600013`

[20] M. Graf, Numerical spherical designs on s2.

[21] M. Graf, Quadrature rules on manifolds.

[22] J. Keiner, S. Kunis, D. Potts, Using nfft3 - a software library for various nonequispaced fast fourier transforms, ACM Trans. math. Software 36 (2009) 1–30.

[23] J. Keiner, S. Kunis, D. Potts, Efficient reconstruction of functions on the sphere from scattered data, Journal of Fourier Analysis and Applications 13 (4) (2007) 435–458. `doi:10.1007/s00041-006-6915-y`.
URL `<GotoISI>://WOS:000248920200007`

[24] C. Maurice, R. Fortunier, A 3d hough transform for indexing ebsd and kossel patterns, Journal of Microscopy 230 (3) (2008) 520–529. `doi:DOI10.1111/j.1365-2818.2008.02045.x`.
URL `<GotoISI>://WOS:000256161300021`

[25] T. Britton, V. Tong, J. Hickey, A. Foden, A. Wilkinson, Astroebsd: exploring new space in pattern indexing with methods launched from an astronomical approach, ArXiv Preprint.
URL `https://arxiv.org/abs/1804.02602`

[26] P. T. Pinard, M. Lagacé, P. Hovington, D. Thibault, R. Gauvin, An open-source engine for the processing of electron backscatter patterns: Ebsd-image, Microscopy and Microanalysis 17 (2) (2011) 374–385. `doi:DOI10.1017/S1431927611000456`.
URL `https://doi.org/10.1017/S1431927611000456`

[27] A. Morawiec, Determination of orientations from monochromatic diffraction patterns as the constellation problem, IOP Conference Series: Materials Science and Engineering 82 (1) (2015) 012008.
URL `http://stacks.iop.org/1757-899X/82/i=1/a=012008`

[28] J. Bassinger, D. Fullwood, J. Kacher, B. Adams, Pattern center determination in electron backscatter diffraction microscopy, Microscopy and Microanalysis 17.

doi:10.1017/S1431927611000389.
URL https://www.cambridge.org/core/journals/microscopy-and-microanalysis/article/pattern-center-determination-in-electron-backscatter-diffraction-microscopy/782ECC7897206E98B86870C1F2EAB780

[29] A. Winkelmann, G. Nolze, M. Vos, F. Salvat-Pujol, W. Werner, Physics-based simulation models for ebsd: advances and challenges, IOP Conference Series: Materials Science and Engineering 109. doi:10.1088/1757-899X/109/1/012018.
URL http://iopscience.iop.org/article/10.1088/1757-899X/109/1/012018/pdf

[30] A. Winkelmann, Dynamical effects of anisotropic inelastic scattering in electron backscatter diffraction, Ultramicroscopydoi:10.1016/j.ultramic.2008.05.002.